INTERNATIONAL JOURNAL FOR NUMERICAL AND ANALYTICAL METHODS IN GEOMECHANICS, VOL. 21, 229–240 (1997)

# CONSEQUENCES OF FLUID LAG IN THREE-DIMENSIONAL HYDRAULIC FRACTURES

S. H. ADVANI*, T. S. LEE[1], R. H. DEAN[2], C. K. PAK[3] AND J. M. AVASTHI[4]

[1]*SOKANG University, Seoul, Korea*
[2]*ARCO E&P Technology Co., Plano, Texas, U.S.A.*
[3]*DAEWOO Advanced Research Institute, Yongin, Korea*
[4]*Chevson Petroleum Technology Co., Houston, Texas, U.S.A.*

## SUMMARY

Research investigations on three-dimensional (3-D) rectangular hydraulic fracture configurations with varying degrees of fluid lag are reported. This paper demonstrates that a 3-D fracture model coupled with fluid lag (a small region of reduced pressure) at the fracture tip can predict very large excess pressure measurements for hydraulic fracture processes. Predictions of fracture propagation based on critical stress intensity factors are extremely sensitive to the pressure profile at the tip of a propagating fracture. This strong sensitivity to the pressure profile at the tip of a hydraulic fracture is more strongly pronounced in 3-D models versus 2-D models because 3-D fractures are clamped at the top and bottom, and pressures in the 3-D fractures that are far removed from the fracture tip have little effect on the stress intensity factor at the fracture tip. This rationale for the excess pressure mechanism is in marked contrast to the crack tip process damage zone assumptions and attendant high rock fracture toughness value hypotheses advanced in the literature. A comparison with field data is presented to illustrate the proposed fracture fluid pressure sensitivity phenomenon. This paper does not attempt to calculate the length of the fluid lag region in a propagating fracture but instead attempts to show that the pressure profile at the tip of the propagating fracture plays a major role in fracture propagation, and this role is magnified in 3-D models. © 1997 by John Wiley & Sons, Ltd. Int. j. numer. anal. methods geomech., vol. 21, 229–240 (1997)

(No. of Figures: 9 No. of Tables: 3 No. of Refs: 17)

Key words: hydraulic fracture; fluid lag; excess pressure

## INTRODUCTION

Progress in hydraulic fracture simulation and design is perhaps best exemplified by the steady evolution from two-dimensional[1,2] to three-dimensional[3–5] modelling. The introduction of important reservoir characteristics such as multi-layering, *in situ* stress contrasts and thermal effects has been facilitated by theoretical and computational developments. However, current 3-D fracture models still commonly underpredict the treatment pressures seen in field applications.

Several arguments have been advanced to explain the existence of 'abnormally' excessive treatment pressures relative to the PKN model deduced pressures in various fracturing operations. Plugging of fractures by fines, poroelasticity, fracture surface waviness, and process-zone-induced fracture toughness enhancement have been cited as contributing factors. Palmer and Veatch[6] and Palmer *et al.*,[7] for example, postulate high friction losses in constricted or branched fractures as a primary source of the excess pressure phenomenon. Consistent with the fluid lag hypothesis, coal fines have been reported at the crack tip[8] as a pressure elevator source. In this

* Deceased

CCC 0363–9061/97/040229–12$17.50

*Received 13 September 1995*
*Revised 4 June 1996*

context, based on an analysis of the fluid lag region in GdK and penny-shaped fractures,[9] only modest pressure increases are evidenced due to crack tip plugging.[10] Relatively small excess pressure ratios are similarly predicted for multiple parallel fractures and deviations in the primary fracture channel.

Shlyapobersky *et al.*[11,12] have computed apparent fracture toughness values of reservoir rocks using net fracture pressure field measurements and two-dimensional fracture mechanics modelling. Their field calibrated (*in situ*) fracture toughness are at least an order of magnitude higher than those determined from rock sample laboratory tests—presumably attributed to fracture toughness enhancement due to random micro-cracking, crack shielding, or elastoplastic behaviour in the process zone, or to a fluid lag region at the fracture tip. Shlyapobersky *et al.* did not attempt to separate the fluid lag effect from the process zone effect, but instead combined the two effects into a single parameter called the apparent fracture toughness. Yew and Liu[13] use the Drucker–Prager failure model to demonstrate an increase in toughness and employ the GdK model to illustrate the importance of a dry fracture zone.

In this paper, it is shown that a small region of reduced pressure at the tip of a propagating fracture can significantly reduce the stress intensity factor for the fracture. Whether this region of reduced pressure is due to the fracture tip running ahead of the fluid front, to excessive fluid leakoff, to friction losses, or to plugging, etc., it is shown that the presence of this region of reduced pressure, referred to here as the fluid lag region, can result in large excess pressures during fracture propagation.

This paper compares 3-D hydraulic fracture results with 2-D GdK results to show that the fully pressurized 3-D solution predicts stress intensity factors that are much smaller than those predicted from 2-D GdK models, and this paper also discusses the similarities between the 3-D fluid lag results presented here and published 2-D GdK fluid lag results. This paper also uses 3-D fluid lag results with a PKN model to show the effect of fluid lag on elongated, propagating fractures. A comparison with Chevron field data is presented to illustrate the fluid-lag-induced pressure sensitivities.

## MODEL FORMULATION AND ANALYSIS

This paper considers a 3-D elongated rectangular crack with a half fracture length, $L$, and half-height, $H$, as shown in Figure 1. We call this a 3-D hydraulic fracture because we are solving a 3-D elastic problem rather than a 2-D elastic problem such as for a GdK-type rectangular fracture. The fracture fluid region is represented by the distance, $L_f$, and the fluid pressure is approximated by an averaged uniform value. This assumption is consistent with the simplifications imposed on selected GdK and Penny-shaped models,[9] even though a logarithmic fluid pressure profile is suggested.

The assumption of an averaged uniform fracture pressure distribution facilitates the analysis and yields a physically realistic model for evaluating the excess pressure phenomenon. The pressure in the fluid lag region is represented by the far-field reservoir pore pressure, $P_\infty$. The effective pressure distribution inside the fracture (Figure 2(a)) can be written as

$$\Delta P = \begin{cases} p - \sigma_0 & \text{for} \quad 0 \leqslant x \leqslant L_f \\ -(\sigma_0 - P_\infty) & \text{for} \quad L_f \leqslant x \leqslant L \end{cases} \tag{1}$$

where $p$ is the average bottomhole fracturing fluid pressure and $\sigma_0$ represents the minimum horizontal *in situ* stress. Alternatively, the effective pressure distribution along the entire crack (Figures 2(b) and 2(c)) can be expressed as

$$\Delta P = \{p - \sigma_0\} - \mathscr{H}(x - L_f)(p - P_\infty) \tag{2}$$

where $x$ is the co-ordinate along the fracture length and $\mathscr{H}(\cdot)$ is the Heaviside step function.

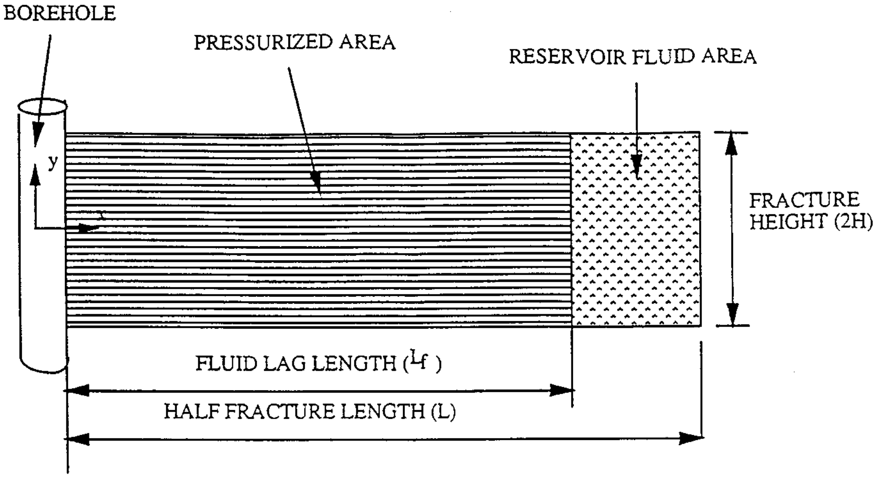


Figure 1. Schematic description of fluid lag in a three-dimensional elongated rectangular crack

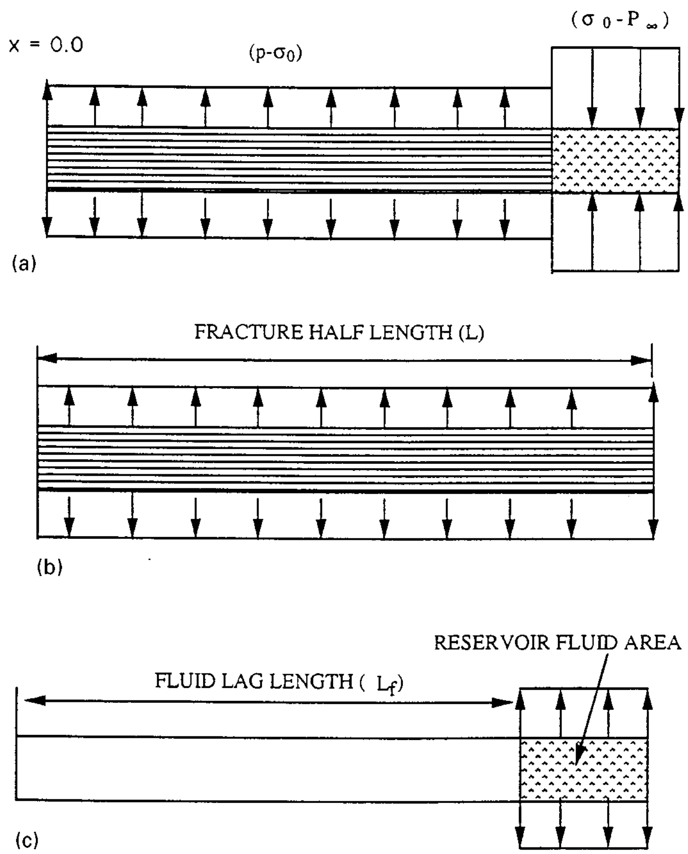


Figure 2. Superposition of loadings for rectangular crack: (a) Effective pressure distribution with fluid lag in rectangular crack; (b) Fully pressurized crack for unit loading corresponding to function $F1$; (c) Partially pressurized crack for unit loading corresponding to function $F2$

A previously developed numerical method, based on the finite element evaluation of the singular integral equation governing an arbitrary planar crack problem,[14] is employed to establish an algebraic equation of the form

$$\Delta P_i = S_{ij} W_j \tag{3}$$

where $\Delta P_i$ and $W_j$ are the nodal values of the effective pressure and opening width, respectively. Inversion of the stiffness matrix, $S_{ij}$, along with the application of the boundary conditions characterized by a zero opening width at the crack front yields the appropriate displacement field for the specified pressure distribution. Once the crack opening width, $W$, is obtained, the Mode I stress intensity factor, $K_{\mathrm{I}}$, is computed from the relation

$$K_{\mathrm{I}} = \frac{G}{4(1-v)} w \left[\frac{2\pi}{d}\right]^{1/2} \tag{4}$$

where $d$ is the distance from the crack front, $G$ is the reservoir shear modulus and $v$ denotes its Poisson's ratio.

A typical finite element model mesh used in the computation of the displacement field associated with the elongated rectangular crack is shown in Figure 3. Triangular three-noded elements are used with a total of 416 elements. A refined mesh is used near the crack tip to obtain convergent solutions. The use of superposition concepts and dimensional analysis eliminates redundant numerical computations. For example, the stress intensity factor, at any given point on the crack surface, can be written as

$$\frac{K_{\mathrm{I}}}{\sqrt{\pi H}} = \Delta P F_1(H/L) - (p - P_{\infty}) F_2(H/L, L_{\mathrm{f}}/L) \tag{5}$$

where $H/L$ and $L_{\mathrm{f}}/L$ represent the crack slenderness and fluid lag length ratios, respectively, and $\Delta P = p - \sigma_0$. The weight or influence functions at a point, $F_1(H/L)$ and $F_2(H/L,\ L_{\mathrm{f}}/L)$ in equation (5), represent the normalized stress intensity factors due to a uniform fluid pressure, and a pressurized region at the fracture tip, respectively. The reader should note that $F_2(H/L,0) = F_1(H/L)$.

Table I reveals the weight function values ($F_1$, $F_2$) at the centre of the advancing crack front ($x = L$, $y = 0$) for cracks with slenderness ratios ranging from 0.1 to 0.4 and different ratios of

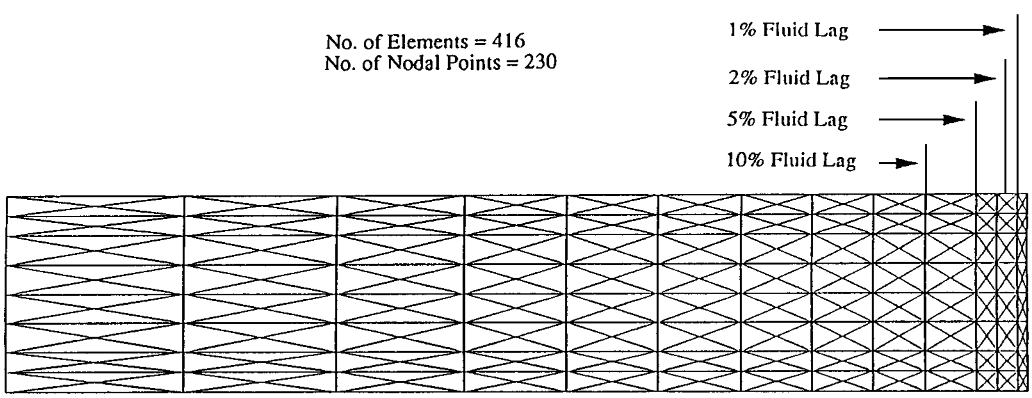


Figure 3. Finite element mesh for rectangular crack

 

Table I. Weight functions ($F_1$, $F_2$) for stress intensity factor computation

| $H/L$ | MODELS | $F_1$ | $F_2$ | | | |
|---|---|---|---|---|---|---|
| | | | $L_f/L = 0{\cdot}90$ | $L_f/L = 0{\cdot}95$ | $L_f/L = 0{\cdot}98$ | $L_f/L = 0{\cdot}99$ |
| 0·1 | ANALYTICAL | | 0·900 | 0·636 | 0·402 | 0·285 |
| | FEM | 0·884 | 0·732 | 0·606 | 0·386 | 0·267 |
| 0·2 | ANALYTICAL | | 0·636 | 0·450 | 0·285 | 0·201 |
| | FEM | 0·905 | 0·611 | 0·477 | 0·289 | 0·199 |
| 0·3 | ANALYTICAL | | 0·520 | 0·367 | 0·232 | 0·164 |
| | FEM | 0·908 | 0·528 | 0·403 | 0·241 | 0·165 |
| 0·4 | ANALYTICAL | | 0·457 | 0·318 | 0·201 | 0·142 |
| | FEM | 0·907 | 0·470 | 0·355 | 0·210 | 0·144 |

fluid lag. Table I presents values of $F_1$ and $F_2$ for a 3-D fracture. The values of $F_1$ in Table I are for a fully pressurized fracture, and are significantly different from the values one would obtain from a plane strain hydraulic fracture model. These differences arise for long 3-D fractures that are closed along the top and bottom because any load on the fracture face that is not near the fracture tip will be supported by the material above and below the fracture rather than being transmitted to the fracture tip. Because of this, length scales for long 3-D fractures should be based on the fracture height rather than on the fracture length. A plane strain hydraulic fracture model such as the GdK model[9] uses the fracture half-length $L$ for computing the stress intensity factor rather than the fracture half-height, $H$. A GdK model replaces $F_1(H/L)$ in Table I by the square root of $L/H$. Consequently, a GdK model employs values of $F_1$ equal to 3·2, 2·2, 1·8, and 1·6 for $H/L$ equal to 0·1, 0·2, 0·3, and 0·4, respectively. These GdK values for $F_1$ are significantly larger than the 3-D values in Table I which are all close to 0·9.

If one were to use plane strain values of $F_1$ to predict fracture propagation, one would significantly underestimate the pressures required for propagation of a long fracture. For example, if we assume that there is no fluid lag, then $F_2$ is zero in equation (5). For the case of $H/L$ equal to 0.1, the ratio of the net pressure $\Delta P$ in 3-D to the net pressure in plane strain is 3·2/0.88, i.e. 3-D computations predict a net pressure that is 3·6 times larger than the plane strain estimate of net pressure for a fully pressurized fracture.

The analytical values of $F_2$ in Table I are obtained from the asymptotic expression of the stress intensity factor, $K_I$, for the case, $L - L_f \ll H$. The crack front near $x = L$, $y = 0$ is then approximately under plane strain conditions since the influence of the fracture corners ($y = +H, -H$) is negligible. Also, the crack can be considered to be semi-infinite in the $x$-direction, considering that $L - L_f \ll H \ll L$. The value of $F_2$, corresponding to unit loading in the fluid lag region, can then be expressed by

$$F_2 = \frac{K_I}{\sqrt{\pi H}} \cong \frac{2}{\pi}\sqrt{\frac{2(L - L_f)}{H}} \approx 0{\cdot}900\sqrt{\frac{L - L_f}{H}} \tag{6}$$

Table I illustrates the comparisons between the FEM and analytically determined values of $F_2$. The analytical approximation for $F_2$ is generally valid for the ranges of $L_f/L$ and $H/L$ selected here. The analytical formula in equation (6) allows one to estimate $F_2$ for values of fluid lag not discussed in this paper and also serves as a validation for the finite element computations. However, all excess pressure calculations performed in this paper employ values of $F_2$ obtained from the finite element computations.

 

Representative plots of the weight functions $F_1$ and $F_2$ for $H/L = 0{\cdot}1$ along the vertical and horizontal edges of the crack tip are shown in Figures 4 and 5. One can see in Figure 5 that along the vertical crack edge $F_2$ approaches $F_1$ fairly quickly as $L_f/L$ decreases. As mentioned earlier, $F_2$ will equal $F_1$ when $L_f$ equals zero. For the fully pressurized case, the results for $F_1(H/L)$ are

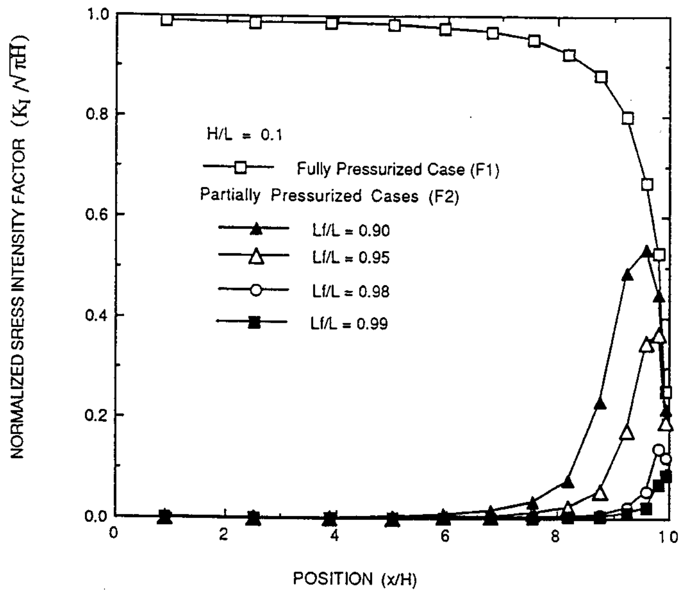


Figure 4. Stress intensity factor weight functions along the horizontal crack edge ($y = +H, -H$)

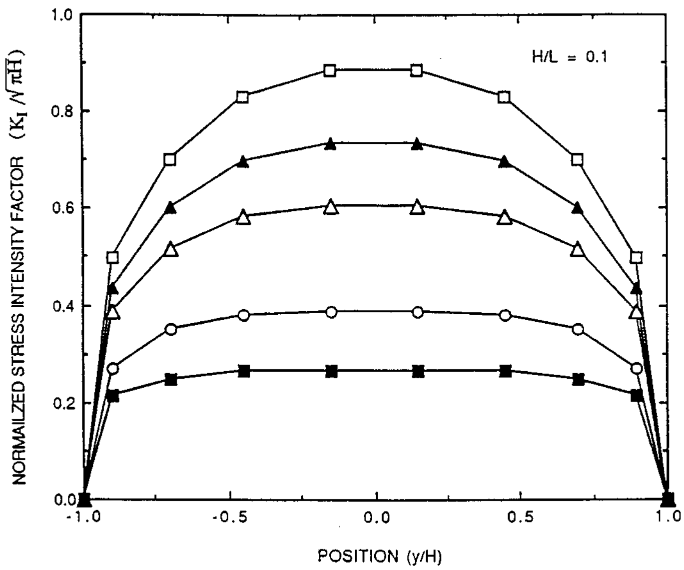


Figure 5. Stress intensity factor weight functions along the vertical crack edge ($x = L$) (note legends in Figure 4)

 

compatible with those obtained by Weaver,[15] using an alternative methodology. Similar trends in the stress intensity factor profiles have also been obtained for $H/L = 0{\cdot}2$, $0{\cdot}3$, and $0{\cdot}4$.

The reader should note that the fully pressurized fracture has a normalized stress intensity factor of 0·88 at the centre of the leading edge of the fracture while the solution with only the last 10 per cent of the fracture pressurized has a normalized stress intensity factor of 0·73. Consequently, for the fully pressurized fracture with $H/L = 0{\cdot}1$, 83 per cent of the normalized stress intensity factor at the fracture tip arises from the pressures in the last 10 per cent of the fracture. Furthermore, since the analytical expression for $F_2$ is a function of $(L - L_f)/H$, this implies that the stress intensity factor at the tip of a long fracture is primarily determined by the pressure profile in the region from $L - H$ to $L$ where $L$ is the fracture half-length and $H$ is the fracture half-height.

## BOTTOMHOLE TREATMENT PRESSURE RESPONSE EVALUATIONS

The bottomhole treatment pressure can be determined from the results in Table I for a specified degree of fluid lag. Comparisons with the pressure values, in the absence of fluid lag, for PKN and 3-D models can also be made to evaluate the excess pressure ratios.

The effective borehole pressure ($\overline{\Delta P}$), with no fluid lag, for a 3-D rectangular fracture is obtained from equation (5) in the form

$$\overline{\Delta P} = \frac{K_{IC}}{F_1\sqrt{\pi H}} \tag{7}$$

where $K_{IC}$ is the reservoir critical stress intensity factor and the values of $F_1$ are presented in Table I. In the presence of fluid lag, the effective pressure ($\Delta P$), normalized with respect to the no-lag effective pressure, obtained from equations (5) and (7), is

$$\frac{\Delta P}{\overline{\Delta P}} = \frac{F_1}{F_1 - F_2}\left\{1 + \frac{(\sigma_0 - P_\infty)}{K_{IC}/\sqrt{\pi H}} F_2\right\} \tag{8}$$

The parameter $R = (\sigma_0 - P_\infty)\sqrt{\pi H}/K_{IC}$ in equation (8) is typically in the range $1 \leqslant R \leqslant 1000$, considering representative values of $\sigma_0 - P_\infty$ (200–6000 psi), total fracture height (10–200 ft), and reservoir fracture toughness (500–2000 psi in$^{1/2}$). Table II presents the effective pressure ratios using the results of Table I for different fracture slenderness ratios ($H/L$), fluid lag length ratios ($L_f/L$) and the non-dimensional parameter, $R$. A graphical representation of these results for $R = 10$ and $R = 500$ is shown in Figures 6 and 7, respectively.

As indicated, the pressure ratio increases dramatically with increased fluid lag. Also, significant pressure sensitivities are evidenced with respect to the normalized *in situ* stress parameter, $R$, and crack slenderness ratio, $H/L$.

Jeffrey[9] has presented 2-D models of fracture propagation using stress intensity factors and fluid lag. The results in Reference 9 were not expressed in the form of equation (8) used in this paper; however, one can express the 2-D results in Reference 9 in the form of equation (8). If this is done, then one finds that the 2-D analysis in Reference 9 predicts that $F_1 = 1{\cdot}0$ and $F_2 = 1 - (2/\pi)\sin^{-1}(L_f/L)$. In addition, Reference 9 uses the fracture half-length $L$ inside the square root in equation (8) rather than the fracture half-height $H$. One finds that for $L_f/L$ near one, there is little difference between the expression for $F_2$ from Reference 9 and the analytical expression for $F_2$ presented in equation (6). In fact, the $F_2$ in equation (6) is the first term in a power series expansion of the $F_2$ from Reference 9. The primary difference between the excess pressures predicted here and those predicted using formulae in Reference 9 arises because of the

Table II. Excessive pressure ($\Delta P/\overline{\Delta P}$) of crack with fluid lag

| $\frac{\sigma_0 - P_\infty}{K_{IC}/\sqrt{\pi H}}$ | $H/L = 0{\cdot}1$ | | | | $H/L = 0{\cdot}2$ | | | |
|---|---|---|---|---|---|---|---|---|
| | $L_f/L = 0{\cdot}9$ | $L_f/L = 0{\cdot}95$ | $L_f/L = 0{\cdot}98$ | $L_f/L = 0{\cdot}99$ | $L_f/L = 0{\cdot}9$ | $L_f/L = 0{\cdot}95$ | $L_f/L = 0{\cdot}98$ | $L_f/L = 0{\cdot}99$ |
| 10·0 | 48·4 | 22·4 | 8·6 | 5·3 | 21·9 | 12·2 | 5·7 | 3·8 |
| 50·0 | 218·7 | 99·5 | 36·0 | 20·6 | 97·1 | 52·5 | 22·7 | 14·0 |
| 100·0 | 431·5 | 195·9 | 70·3 | 39·7 | 191·2 | 103·0 | 43·9 | 26·8 |
| 500·0 | 2134·4 | 966·7 | 344·4 | 192·7 | 943·5 | 506·4 | 213·8 | 128·8 |
| 1000·0 | 4263·0 | 1930·2 | 687·0 | 384·0 | 1883·9 | 1010·7 | 426·1 | 256·4 |
| $\frac{\sigma_0 - P_\infty}{K_{IC}/\sqrt{\pi H}}$ | $H/L = 0{\cdot}3$ | | | | $H/L = 0{\cdot}4$ | | | |
| | $L_f/L = 0{\cdot}9$ | $L_f/L = 0{\cdot}95$ | $L_f/L = 0{\cdot}98$ | $L_f/L = 0{\cdot}99$ | $L_f/L = 0{\cdot}9$ | $L_f/L = 0{\cdot}95$ | $L_f/L = 0{\cdot}98$ | $L_f/L = 0{\cdot}99$ |
| 10·0 | 15·0 | 9·0 | 4·6 | 3·2 | 11·8 | 7·5 | 4·0 | 2·9 |
| 50·0 | 65·5 | 38·0 | 17·8 | 11·3 | 50·9 | 30·8 | 15·0 | 9·7 |
| 100·0 | 128·6 | 74·3 | 34·2 | 21·4 | 99·6 | 60·0 | 28·6 | 18·3 |
| 500·0 | 633·2 | 364·1 | 165·4 | 102·0 | 489·8 | 293·3 | 137·9 | 86·8 |
| 1000·0 | 1264·0 | 726·4 | 329·4 | 202·9 | 977·6 | 584·9 | 274·6 | 172·4 |

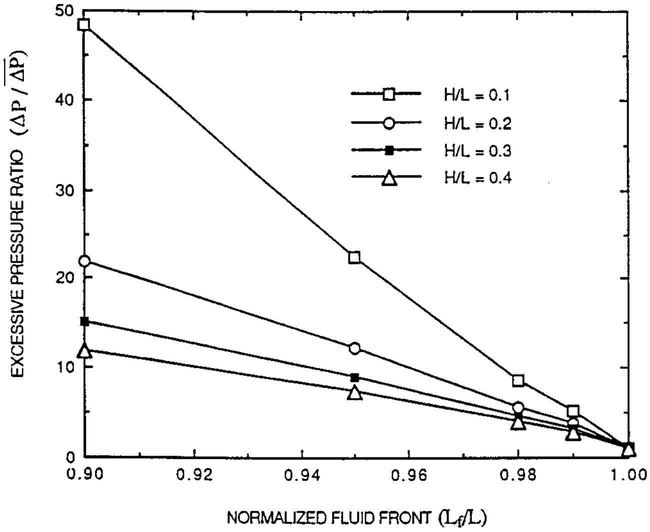


Figure 6. Computed pressure ratios for crack propagation $[(\sigma_0 - P_\infty)/(K_I/\sqrt{\pi H}) = 10{\cdot}0]$

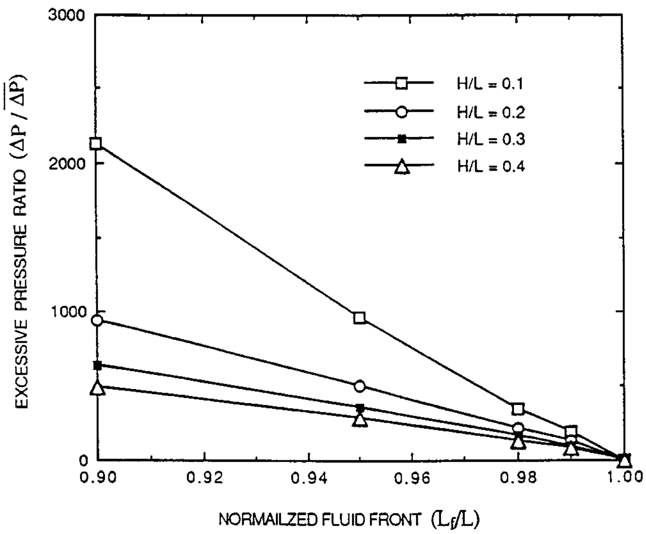


Figure 7. Computed pressure ratios for crack propagation $[(\sigma_0 - P_\infty)/(K_I/\sqrt{\pi H}) = 500{\cdot}0]$

use of $H$ in place of $L$. This use of $H$ in place of $L$ occurs in equation (8) when comparing the fluid lag solution to the fully pressurized solution, and the substitution of $H$ for $L$ also occurs in the expression for the fully pressurized solution given by equation (7). Equation (7) is the same as equation (17) in Reference 9 with $F_1 = 1{\cdot}0$ and $L$ in equation (17) replaced by $H$. The 2-D fluid lag calculations of Barenblatt[16] contain an expression that is similar to $F_2$ listed above for Jeffrey[9]. Barenblatt required that the stresses be finite at the crack tip and found that the crack length could be expressed as $L = L_f[\sin(\pi\sigma_0/2p)]^{-1}$ where $p$ was the fluid pressure in the crack.

## CASE STUDY

A field case (California Experiment Case 3, Table III) provided by Chevron is selected to demonstrate the consequences of fluid lag. This case corresponds to a well-contained elongated fracture. The measured bottomhole treatment pressure history and corresponding pressures predicted by a two-dimensional PKN finite element model are illustrated in Figure 8. Even though the PKN model is a 2-D model, it predicts treatment pressures that are similar to the pressure predictions for more rigorous 3-D models[17] when a fracture is well-contained and the fracture length is larger than the fracture height.

The discrepancy between the pressure responses in Figure 8 can be qualitatively attributed to fluid lag (pressure drop at the fracture tip). The plots in Figure 9 present the effective pressure ratios versus fracture slenderness ratios corresponding to $K_{IC} = 500$ psi in$^{1/2}$, $H = 80$ ft and $\sigma_0 - P_\infty = 325$ psi. The effective pressures in Figure 9 are normalized with respect to the 2-D PKN model pressures corresponding to the time step solutions. The fracture slenderness ratios are directly computed from the payzone height and PKN predicted fracture length responses. The trends in Figure 9 suggest that a fluid lag of approximately 1 per cent may be the source of the significantly elevated measured pressures.

Table III. Treatment data for the case study (California experimental case 3)

| | |
|---|---|
| Young's modulus ($E$) | 2·0E5 psi |
| Poisson's ratio ($n$) | 0·2 |
| Fracture toughness ($K_{IC}$) | 500·0 psi in$^{1/2}$ |
| Leak-off coefficient ($C_L$) | 0·001 ft min$^{1/2}$ |
| Fluid behaviour index ($n'$) | 0·618 |
| Consistency index ($k'$) | 0·0332 Ibf-s$^{n'}$/ft$^2$ |
| Payzone height ($2H$) | 160·0 ft |
| Injection rate ($i_0$) | 46·0 BPM |
| *In situ* stress ($\sigma_0$) | 1175·0 psi |
| Reservoir pressure ($P_\infty$) | 850·0 psi |

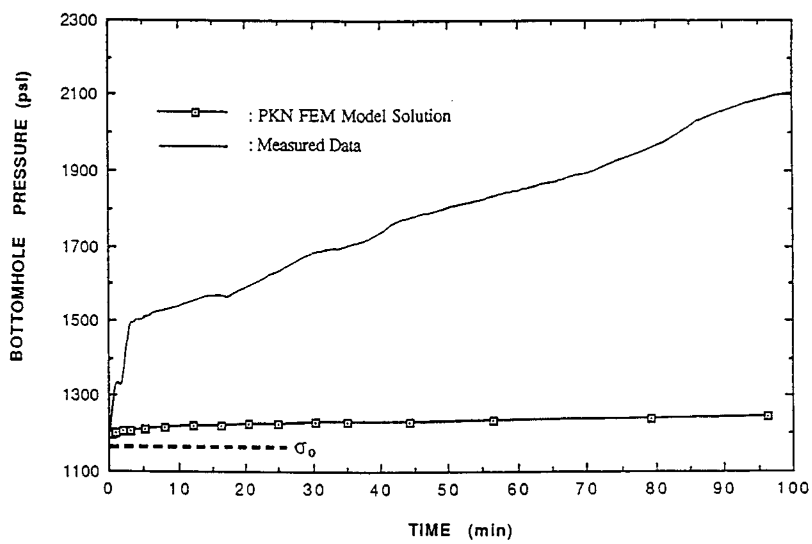


Figure 8. Measured and computed PKN model bottomhole pressure responses (without fluid lag)

 

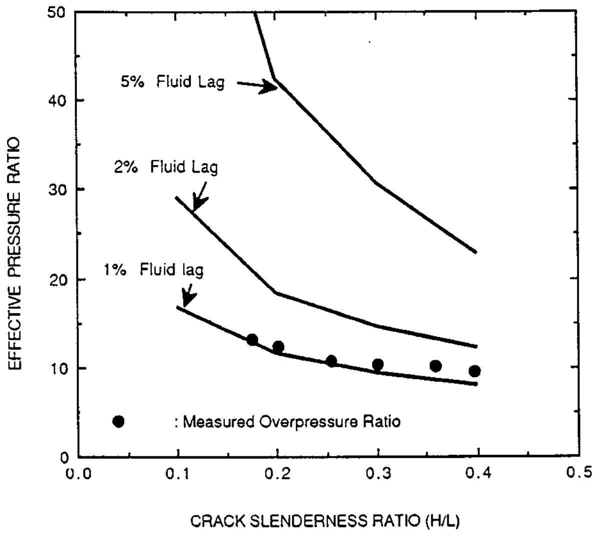


Figure 9. Effective pressure ratio comparisons for case study

## CONCLUDING REMARKS

In contrast with previously reported plane strain and penny-shaped hydraulic fracture model studies, stress intensity factor computations for 3-D, fully and partially pressurized rectangular cracks are detailed. Finite element computations are validated with published results[15] and against an analytical approximation. Using these results, it is shown that the pressure distribution near the tip (within one half-height of the fracture tip) of a long fracture plays a dominant role in determining the stress intensity factor at the tip of that fracture. This dominance of the pressure profile at the fracture tip suggests that fluid lag, or any mechanism that causes a region of reduced pressure at a fracture tip, can easily result in the excess pressure phenomenon observed in hydraulic fracture treatments. These same effects will be much less important in radial and 2-D, GdK-type rectangular fracture models where all loads on the fracture surface are easily transmitted to the tip of a propagating fracture. Sensitivities are presented for various degrees of fluid lag and it is shown that a small amount of fluid lag creates a very large increase in the pressures needed for fracture propagation. Limited verification of the fluid lag hypothesis is demonstrated through the analysis of field data.

The dominance of the pressure profile in a small region near a fracture tip suggests how one might modify plane strain estimates of stress intensity factors to include 3-D effects in long rectangular fractures. It is recommended that plane strain computations should use pressures near the fracture tip (within one fracture height of the tip) as the loading parameter for the fracture surface and should use the fracture height as the length scale in computing estimates of stress intensity factors. The fracture height rather than the fracture half-height is suggested here to account for the fact that there is some contribution to the stress intensity factor for those regions of the fracture that lie more than a half-height distance from the fracture tip.

## ACKNOWLEDGEMENTS

This effort was partially supported by the Chevron Oil Field Research Co. and Cray Research Inc. Computational facilities were provided by the Lehigh University Computer Center. This

 

paper was originally presented as SPE 25888 at the 1993 SPE Rocky Mountain Regional/Low Permeability Reservoirs Symposium held April 12–14 in Denver.

## REFERENCES


1. T. K. Perkins and L. R. Kern, 'Widths of hydraulic fractures', *JPT*, **13,** 937–949 (1961). Also see R. P. Nordgren, 'Propagation of a vertical hydraulic frcture,' *SPE J.* **253,** 306–314 (1972).
2. J. Geertsma and F. de Klerk, 'A rapid method of predicting width and extent of hydraulically induced fractures', *JPT*, **246,** 1571–1581 (1969).
3. R. J. Clifton and A. S. Abou–Sayed, 'A variational approach to the prediction of the three-dimensional geometry of hydraulic fractures', *SPE Paper No. 9878*, *Proc. SPE/DOE Symp. on Low Permeability*, Denver, 1981.
4. M. P. Cleary, M. Kavvadas and K. Y. Lam, 'Development of a fully three-dimensional simulator for analysis and design of hydraulic fracturing', *SPE Paper No. 11631*, *Proc. SPE/DOE Symp. on Low Permeability*, Denver, 1983.
5. S. H. Advani, T. S. Lee, and J. K. Lee, 'Three-dimensional modeling of hydraulic fractures in layered media: Part I–finite elemet formulations', *ASME J. Energy Resources Techol.*, **112,** 1–9 (1990).
6. I. D., Palmer and R. W. Veatch Jr., 'Abnormally high fracturing pressures in step-rate tests', *SPE Paper No. 16902*, 1987.
7. I. D. Palmer, M. W. Davids and S. J. Jeu, 'Analysis of unconventional behavior observed during coalbed fracturing treatments', *Proc. 1989 Coalbed Methane Symp.*, The University of Alabama/Tuscaloosa, 1989, pp. 395–415.
8. G. J. Bell, A. H. Jones, R. H. Morales and R. A. Schraufnagel, 'Coal seam hydraulic fracture propagation on a laboratory scale', *Proc. 1989 Coalbed Methane Symp.*, The University of Alabama/Tuscaloosa, 1989, pp. 417–425.
9. R. G. Jeffrey, 'The combined effect of fluid lag and fracture toughness on hydraulic fracture propagation', *SPE Paper No. 18957*, *Joint Rocky Mountain Regional/Low Permeability Reservoirs Symp.*, Denver, March 1989.
10. R. G. Jeffrey, J. J. Hinkel, K. H. Nimerick and J. McLennan, 'Hydraulic fracturing to enhance production of methane from coal seams', *Proc. 1989 Coalbed Methane Symp.*, The University of Alabama/Tuscaloosa, 1989, pp. 385–394.
11. J. Shlyapobersky, G. K. Wong and W. W. Walhaug, 'Overpressure calibrated design of hydraulic fracture simulations', *SPE Paper No. 18194,* 1988.
12. J. Shlyapobersky, W. W. Walhaug, R. E. Sheffield and P. T. Huckabee, 'Field determination of fracturing parameters for overpressure calibrated design of hydraulic fracturing', *SPE Paper No. 18195,* 1988.
13. C. H. Yew and G. Liu, 'The fracture tip and $K_{IC}$ of a hydraulically induced fracture', *SPE Paper No. 22875, The 66th Annual Technical Conf. and Exhibition*, Dallas, 6–9 October 1991.
14. T. S., Lee, S. H. Advani and J. K. Lee, 'Indirect finite element evaluation of two-dimensional finite part integral using Fourier transformation', *Int. j. numer methods eng.* **36,** 2981–2996 (1993).
15. J. Weaver, 'Three-dimensional crack analysis', *Int. J. Solids Struct.*, **13,** 321–330 (1977).
16. G. I. Barenblatt, 'The mathematical theory of equilibrium cracks in brittle fracture', in *Advances in Applied Mechanics*, Vol. 7, 1962, pp. 55–129.
17. R. J. Clifton, 'Three-dimensional fracture propagation models', in: *Recent Advances in Hydraulic Fracturing.* Monograph Series, SPE, 1989, pp. 95–108.